Electrochemical Materials and Technologies

ARTICLE

Electrochemical Materials and Technologies

eISSN: 2949-0561

Cite this: Electrochem. Mater. Technol. 4 (2025) 20254050

# Development of heat transfer and electric current models of anode on the base of NiO-$Li_2O$ ceramics

Ksenia Abramova [a, b *], Andrey Anisimov [a], Oksana Rakhmanova [a, b], Dmitry Maksimov [a], Alexander Kosov [a], Yuri Mochalov [c], Sergei Nikiforov [d], Yuri Zaikov [a, b]

Received: 25 December 2024
Accepted: 11 March 2025
Published online: 18 March 2025

DOI: 10.15826/elmattech.2025.4.050

In this paper, the finite element method in COMSOL Multiphysics is employed to numerically simulate the electric field in a construction consisting of a ceramic NiO-$Li_2O$ (3 wt. %) anode attached to two steel current leads, as well as the thermal fields within a quartz cell containing this construction. The distributions of the electric current density and temperature gradient generated in the ceramic anode when the applied current is 10 to 50 A (in 10 A increments) are calculated. The model is validated using experimental data. The main causes of anode cracking at the point where it is attached to the current lead are identified. Using the proposed model, the electric field distribution in a similar anode with a new current lead design is predicted. It is demonstrated that the new current lead design allows minimizing the disparity in current density values between the area under the current lead and the free part of the anode.

**keywords:** finite element method, ceramic anode, thermal conductivity, electrical conductivity, mathematical modeling



## 1. Introduction

Today, the nuclear industry holds a leading position in electricity production. On the one hand, the high interest in this sector creates a continuous need to optimize existing technologies and to introduce new ones. On the other hand, the increasing energy consumption each year intensifies the urgent problem of radioactive waste (RW) accumulation. Addressing the challenges related to RW disposal requires the development of closed nuclear cycle technologies, particularly in the area of pyrochemical processing [1]. The core of this approach is the repetitive extraction of U, Pu, and rare earth metals (REM) from spent nuclear fuel (SNF) using the electrochemical method in halide and oxide-halide melts at high temperatures [2]. The successful industrial implementation of the electrochemical SNF recovery technology is linked to the search for suitable structural materials that can operate in oxide-halide melts without generating impurities that would contaminate the melt and the cathode product [3].

Particular attention should be given to the search for an anode material that meets a number of requirements for operation in the electrochemical reduction of SNF [4]. The study [5] reports the advantage of NiO-$Li_2O$ ceramics over traditional inert metal electrodes. The authors note the high corrosion resistance and inertness of the material in oxide-halide melts within the operating temperature range of 823–923 K. However, preliminary tests of ceramic anodes indicate that cracking occurs at the points where the anode is attached to the current lead, which can significantly reduce its service life and increase costs (including those of RW disposal). Identifying the causes of this phenomenon will contribute to the rapid

a: Institute of High-Temperature Electrochemistry, Ural Branch of Russian Academy of Sciences, Yekaterinburg 620990, Russia
b: Ural Federal University named after the first President of Russia B.N. Yeltsin Yekaterinburg 620002, Russia
c: Joint-Stock Company «Proryv», Moscow 140120, Russia
d: Limited Liability Company «Electrochemical generation» Yekaterinburg 620091, Russia

* Corresponding author: abramova@ihte.ru

development of pyrochemical reprocessing technology for SNF.

The problem of finding materials and optimal design solutions in the development of new technologies is a crucial aspect of the complex theoretical and experimental challenges that should be addressed before the implementation stage in industrial production. The search for suitable materials for SNF processing is a labor-intensive, time-consuming, and resource-intensive issue, complicated by the necessity of conducting research in a controlled atmosphere, at high temperatures, and in the presence of radiation exposure. Therefore, the development of numerical models for devices and structural elements used in high-temperature processes is beneficial for reducing the time spent on experimental work.

The study of hydro- and gas-dynamic flows, as well as the mechanical strength of structures during their operation, is a traditional and well-established area for the application of numerical modeling methods [6–8]. As computing resources improve, numerical modeling is increasingly utilized to investigate more complex processes associated with multiphysical problems, including thermomechanical effects [9], electrochemical and physicochemical processes in porous and multilayer conductive microstructures [10, 11], and more.

An important trend in numerical modeling is the development of models for selecting optimal operating modes for industrial, semi-industrial, and laboratory cells, where the operating conditions of such systems are reproduced. For example, in [12] a basic model of an electrolysis cell for aluminum production is presented. The model defines the characteristics of the electromagnetic field generated during operation of the cell under the influence of high currents (200–600 kA), as well as the parameters of magnetohydrodynamic forced convective flows in the electrolyte and at the electrolyte-liquid electrode boundary. The results can be used to optimize the designs of existing electrolyzers.

A coupled mechanical-electrochemical model in COMSOL Multiphysics, as presented in [13], is suitable for calculating the voltage profiles, volume change, porosity, and pressure of pouch cell upon the charge/discharge process of lithium-ion batteries with a composite Si–C anode and predicting the future design of batteries with high energy density and improved safety. Other successful applications of the finite element method in COMSOL Multiphysics are models describing the time-dependent properties of a sacrificial anode for cathodic protection of screw-pile foundations [14], the design of anodes for the hard chrome plating of components with complex geometry [15], and the corrosion of anodes in the electrodeposition of non-ferrous coatings [16].

The aim of the present work is to develop a mathematical model using the COMSOL Multiphysics package [17] that describes the behavior of a ceramic NiO-$Li_2O$ (3 wt. %) anode with two steel current leads during electrical and thermal tests conducted within an argon-filled quartz cell. This model will help clarify the reasons behind the experimentally observed fracture of the anodes near the attachment to the current lead.

## 2. Experimental

The general view of the experimental cell used to conduct the thermal tests of the anode is illustrated in Figure 1 a. The cell is constructed using a quartz glass with a height of 500 mm. Inside the cell, there is a ceramic NiO-$Li_2O$ (3 wt. %) anode. The ends of the anode are connected to current leads that are made of heat-resistant high-alloy stainless steel. The upper current lead clamp allows the supply of current from the positive contact of the PSW7 30-72 current source (manufactured by GW Instek, Taiwan). The lower current lead is connected to the negative contact via a copper busbar. Before the experiment, the cell was half-immersed in a shaft furnace. The upper section of the cell was thermally insulated with kaolin wool and lightweight fireclay brick (brand SHL-I). The cell was connected to a 35-liter vessel to compensate for the thermal expansion of the gas. Subsequently, the cell was evacuated to a residual pressure of 5 Pa and filled with argon. This operation was repeated twice to establish a high-purity argon atmosphere. The temperature of the anode and current leads at the points indicated in Figure 1 b was monitored using twelve chromel-alumel thermocouples (type K). The furnace was heated at a rate of 50 K/h to 923 K. After reaching this temperature, the furnace temperature, the cell position, and the configuration of the thermal insulation of the upper part of the cell were adjusted so that the temperatures at the lower and upper points of the anode (according to the reading from TC2 and TC11, respectively) were 923 and 823 K, respectively.

During the experiment, an electric current (10, 20, 30, 40 or 50 A) was passed through the anode until temperature equilibrium was established at each current load. We considered equilibrium to be achieved if the changes in the thermocouple readings were less than 2 K in 15 minutes. The current was then switched off, and we waited until all thermocouples displayed temperatures corresponding to those at the beginning of the experiment. After this, the experiment was repeated at a higher current value. Temperature readings from the

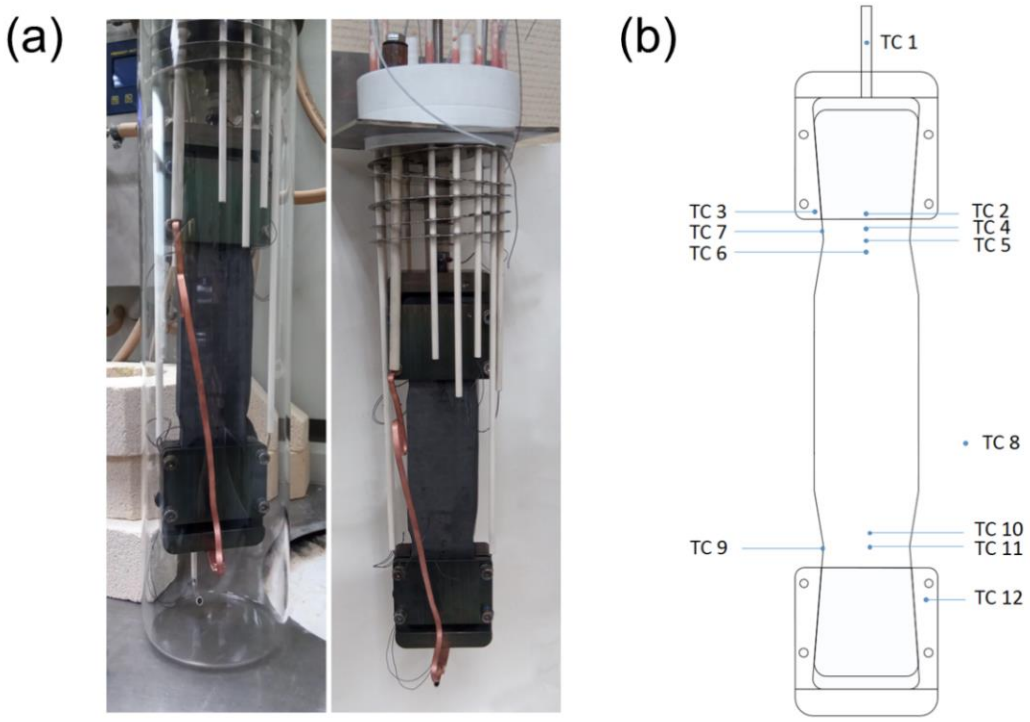


**Figure 1** Experimental cell for conducting thermal tests of ceramic anode: (a) anode assembly, and (b) thermocouple's location diagram.

thermocouples were recorded automatically at 5-second intervals.

During testing of the proposed design, cracking of the anode is detected at the point of attachment to the upper current lead (Figure 2). The reasons for the fracture are unclear and may include the following:

- compression of brittle ceramics when subjected to high currents (exceeding 10 A) due to the difference in the thermal expansion coefficients of the anode and current lead materials;
- development of local overheating at the point of contact between the ceramics and the current lead;
- chemical processes occurring at the contact boundary between the ceramics and the current lead.

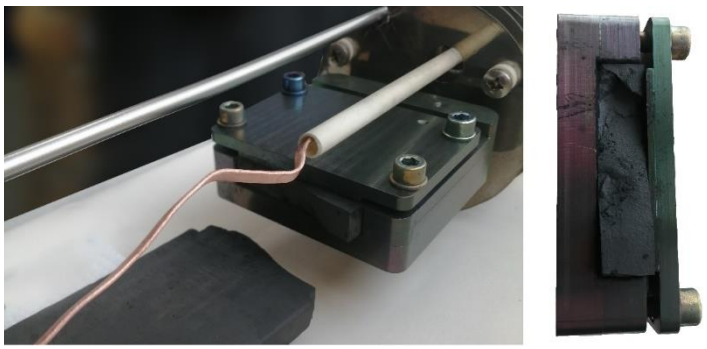

**Figure 2** Ceramic anode failure that occurred during thermal testing in an experimental cell with a current of 50 A.

## 3. Simulation

### 3.1. Geometrical model and materials

The geometric model of the experimental cell is shown in Figure 3. The model considers only the internal space of the cell, excluding quartz glass.

The description of the model domains corresponding to the experimental conditions is given in Table 1. The temperature dependences of the properties of these materials (Appendix A) were utilized in the model to calculate the thermal and electrical distributions.

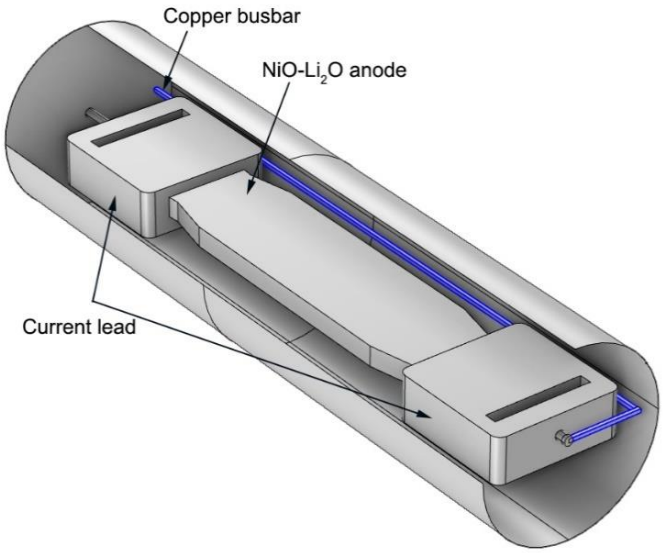


**Figure 3** Geometrical 3D model of the simulation cell.

**Table 1 –** Materials applying in the model.

| Domain | Material |
|---|---|
| Fluid | Argon |
| Current supply (upper and lower) | Steel |
| Anode | Ceramic NiO-$Li_2O$ (3 wt. %) |
| Current-conducting busbar | Copper |

### 3.2. Mathematical model

The developed model described the process of heat exchange inside a quartz cell filled with argon, when it was placed in a shaft furnace. Current of different magnitudes was passed through the anode fixed to the current lead, which was accompanied by heat generation and was implemented using the Electromagnetic Heating multiphysical coupling of two physical interfaces Electric Currents and Heat Transfer in Solids and Fluids, heat generation in conductive domains was described by the Joule-Lenz equation.

To describe mass transfer under natural convection conditions, the Nonisotermal Flow multiphysical coupling was used. In order to determine the gas flow regime, as well as the contribution of convection to heat transfer between solids and the gas domain, the dimensionless criteria Ra, Nu describing the gas flow regime under heat transfer conditions [18] were preliminarily determined.

The Rayleigh number ($Ra$) is a dimensionless quantity and is defined as:

$$Ra = \frac{g \cdot \beta \cdot \Delta T \cdot L^3}{\eta \cdot a}, \quad (1)$$

where $g$ = 9.81 m/s² – gravitational acceleration; $\beta = 3.67 \cdot 10^{-3}$ 1/K – thermal expansion coefficient of argon; $\Delta T$ – temperature gradient in the cell, K; $L$ – the characteristic size of the fluid region, m; $\eta$ – kinematic viscosity of the liquid, Pa · s; $a$ – thermal diffusivity, m²/s.

In the case of argon circulating along a vertical wall 500 mm high under a temperature gradient of 200 K, the value of the $Ra$ criterion is approximately $6 \cdot 10^7$. It is known from the literature that a developed turbulent regime is characterized by values of $Ra > 10^9$; in our case, we used the common turbulent gas flow model RANS (Reynolds-averaged Navier–Stokes equations) in the *k-ε* approximation [19]. According to the calculation results, the average gas circulation velocity inside the cell is $u$ = 0.25 m/s, while the Peclet number ($Pe$) is a criterion that determines the characterizing heat exchange processes between the fluid and the streamlined body:

$$Pe = \frac{u \cdot L}{a}, \quad (2)$$

$Pe$ is approximately 800. Large values of the Peclet number indicate the predominance of convective heat transfer.

To determine the contribution to the heat transfer process between the mechanisms of conduction and convection, the Nusselt number ($Nu$) was determined. In the case of a vertical wall and $Ra < 10^9$, $Nu$ can be calculated as [18]:

$$Nu = 0.68 + \frac{0.67 Ra^{1/4}}{\left[1+\left(\frac{0.492}{Pr}\right)^{9/16}\right]^{4/9}}, \quad (3)$$

where $Ra = 6 \cdot 10^7$ – Rayleigh number, $Pr = \eta \cdot C_p / \rho = 0.05$ – Prandtl number. The Nusselt number in this case is approximately equal to 30. As is known, at $Nu > 20$ one can speak of turbulent flow under conditions of developed convective heat flow [18]. To improve the convergence, the equation of gas motion – the Navier-Stokes equation, was solved in the Boussinesq approximation. This model treats density as a constant value in all solved equations, except for the buoyancy term ($F_b$) in the momentum equation [20, 21].

$$F_b = -\rho_0 g \beta (T - T_o), \quad (4)$$

where $\rho_0$ – reference value of density at $T_o$, kg/m³; $T_o$ – operating temperature of argon, K. In our case, the average temperature in the volume can be taken as the operating temperature, $(T_h + T_c)/2$ = 873 K. At the temperature $T = T_c$, the buoyancy term order then will be equal to 0.36.

The Boussinesq approximation is accurate as long as changes in actual density are small; specifically, the approximation is valid when $\beta(T - T_o) << 1$.

In our case $\beta(T - T_o) \approx 0.36 < 1$, we did not pursue the goal of an accurate description of argon flows inside the cell, we needed to ensure the heat exchange associated with convection, therefore, to improve the convergence, we used the Boussinesq approximation.

### 3.3. Boundary conditions

The main objective of this work was to investigate the contact surface "anode-current lead" and determine the possibility of local overheating when current flows through the conductive domains. For this purpose, we defined special boundary conditions, which were based on the available experimental data of thermal fields in the cell. The definition of special boundary conditions also

allowed us to exclude thermal insulation elements from the model.

An electric current of 10–50 A was supplied through the upper current lead-in with a step of 10 A. At the end of the copper busbar, the condition of electrical grounding ($E$ = 0 V) was defined. At the outer boundaries of the anode and current leads, the condition of electrical insulation was also defined.

Heating from the furnace in the model was carried out by defining the boundary condition of constant temperature $T_h$ = 923 K, this boundary condition acted along the $Oy$ axis, on the outer boundary of the gas domain in the interval 0 < $y$ < 250 mm. In the interval $y$ > 250 mm, a constant temperature $T_c$ = 723 K was determined. The temperatures corresponded to the experimentally measured data.

On the free surfaces of the current lead, as well as on the free surface of the anode, the condition of Surface Emissivity was determined:

$$-\boldsymbol{n}\cdot\boldsymbol{q_r} = \varepsilon\sigma(T_a^4 - T_b^4), \quad (5)$$

where $n$ – surface normal vector; $q_r$ – power flow due to radiation, W/m²; $\varepsilon$ – thermal emissivity coefficient; $\sigma$ = 5.67 · 10⁻⁸ W/(m² · K⁴) – Stefan-Boltzmann constant; $T_a$, $T_b$ – temperature of the receiving and radiating surfaces, K.

On average, the temperature of the free surfaces was constant; the temperature difference was observed only at the contact point of the surfaces. The emissivity coefficients $\varepsilon$ were assumed to be constant and measured with a pyrometer on individual material samples and were 0.3 and 0.8 for steel and ceramics, respectively. The upper and lower parts of the simulation cell had thermal insulation conditions; the boundary conditions of the heat transfer problem are shown in Figure 4.

The argon velocity field was calculated using the Turbulent Flow physical interface, with the Boussinesq approximation. The slip condition was determined on the walls of the simulation cell:

$$\boldsymbol{n}\cdot\boldsymbol{u} = 0. \quad (6)$$

On the outer surfaces of the anode, current leads, and on the upper and lower covers of the simulation cell, the No slip conditions were determined (the tangential component of the velocity $u_\tau$ is not zero on the walls):

$$\boldsymbol{n}\cdot\boldsymbol{u} = 0; \boldsymbol{u_\tau} \neq 0. \quad (7)$$

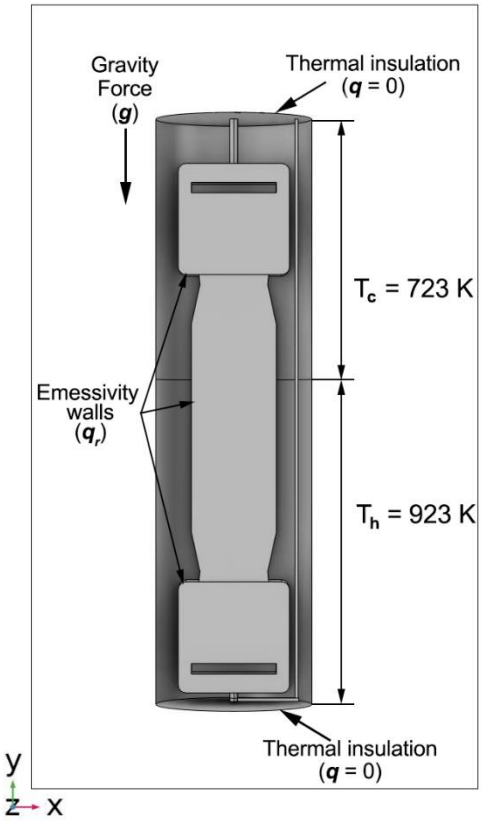


**Figure 4** Boundary conditions of the heat transfer problem.

### 3.4. Model validation

The developed model was validated using data obtained from the experiment, where temperature values were determined using thermocouples placed at key points in the structure (Figure 5 a). Figure 5 b illustrates the good agreement between the temperature values measured in the experiment and those calculated using the model at the corresponding points in the model, specifically when passing currents of 10, 20, and 30 A.

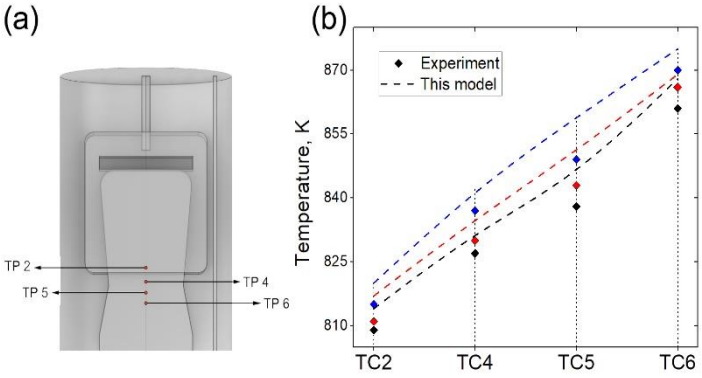


**Figure 5** Results of the anode model validation: (a) – diagram of the arrangement of experimental thermocouples (TC); (b) – comparison of measured (experiment) and calculated (this model) temperatures at the points indicated in Figure 4 a. Temperature data are shown for currents of 10 A (in black), 20 A (in red) and 30 A (in blue).

Validating the model was essential to account for all heat losses present in the experimental setup. Validation of the temperature distribution between the experimental system and its model allowed us to eliminate the necessity of both constructing thermal insulation and performing thermal process calculations within it. This optimization reduced computation time and simplified working with the model.

## 4. Results

All calculations utilizing the proposed model were conducted in a steady-state regime. The current density distribution across the surface of the current lead and the anode, along with the current density dispersion within the corresponding domains, is illustrated in Figure 6.

Figure 6 indicates that the current density distribution on the anode surface is non-uniform, with the highest values ($\approx 2.5 \cdot 10^4$ A/m$^2$) occurring just below the area of contact with the current lead. In the given configuration of the current lead, the current predominantly flows through the more conductive domain – the steel current lead – before transitioning into the volume of the ceramic electrode at the three-phase boundary between argon, the current lead, and the anode. Consequently, high current densities can be reached at this boundary, potentially leading to localized overheating of the ceramic material.

The assessment of the localized overheating beneath the current lead was carried out using a thermal model that accounted for the thermal conductivity of the domains, the heat exchange between them due to thermal radiation, and the convective mixing of argon. The distribution of the temperature field, the velocity of argon during convective mixing, and the direction of the convective flows at $I$ = 30 A are presented in Figure 7.

Figure 7 demonstrates that the highest temperature (923 K) is observed in the lower part of the structure, submerged in the furnace. Near the three-phase boundary, temperatures are lower, ranging from 829 to 852 K. The figure also shows that regions of low gas medium velocity correspond to areas with the highest temperatures. The presence of convective mixing of the gas medium, acting as an additional mechanism for heat exchange, results in the extension of the temperature gradient along the height of the anode.

However, the distribution of the temperature gradient developing within the anode material shows that, despite the general homogeneity in the temperature distribution across the surface of the electrode, the maximum temperature gradient of 8 K/mm occurs at the junction of the anode and the current lead (Figure 8).

Figure 9 presents more detailed isothermal surfaces in the "anode-current lead" region when a current of 50 A flows through the electrode. It is noteworthy that the anode beneath the current lead is significantly cooler than its lower portion. The primary mechanism of heat transfer in this area is the thermal conductivity of the material. Since the thermal conductivity of steel is several times higher than that of the ceramics, the steel current lead serves as a rapid heat dissipation node.

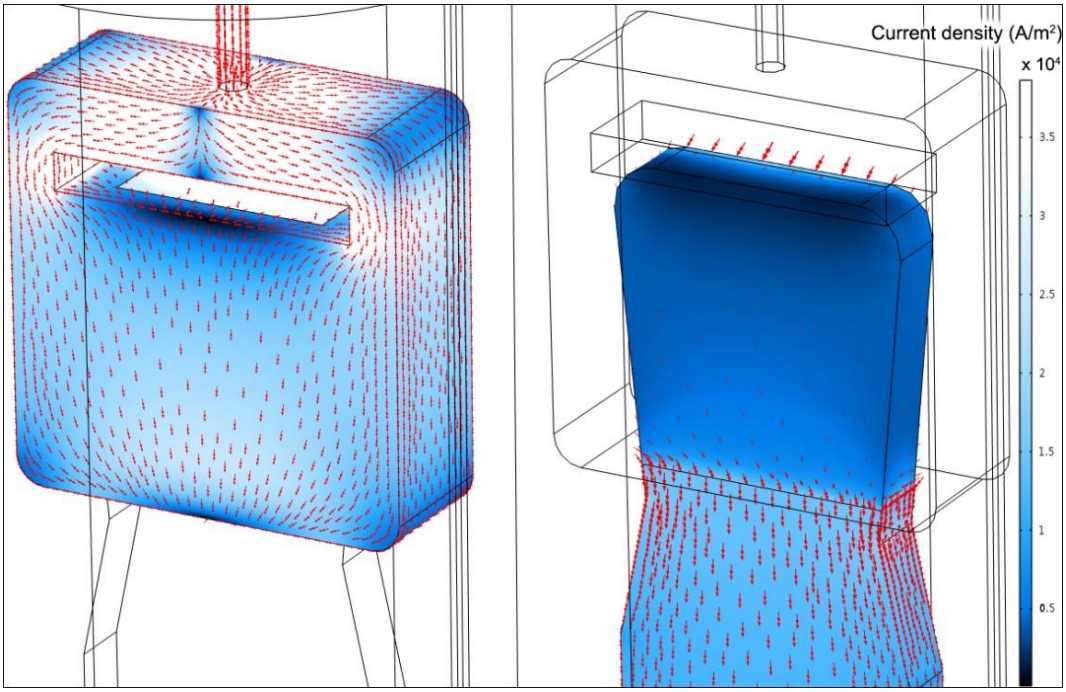


**Figure 6** Distribution of the electric current density on the surface of the current lead (left) and the anode (right). The red arrows indicate the dispersion of current density throughout the volume of the domains. The supplied current is 10 A.

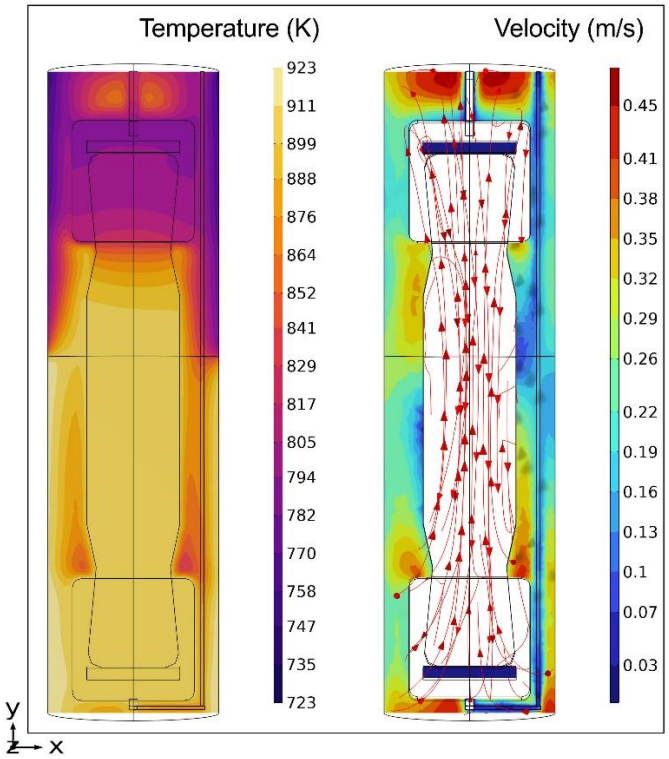


**Figure 7** Temperature distribution field (left) and argon velocity (right) inside the quartz cell during convective mixing. The red arrows indicate the direction of the convective heat flow (W/m³). Current is 30 A.

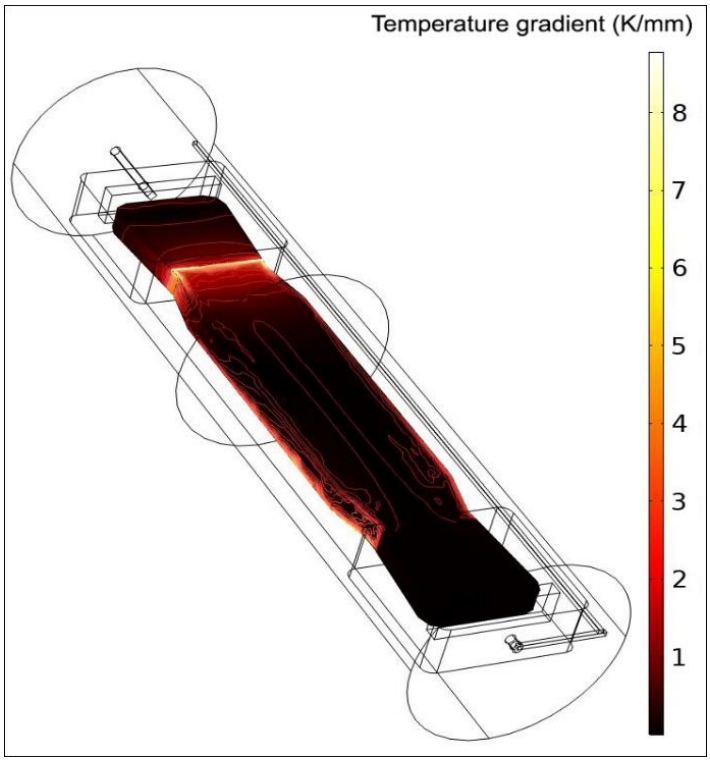


**Figure 8** Temperature gradient developing during the passage of a current of 50 A through the anode.

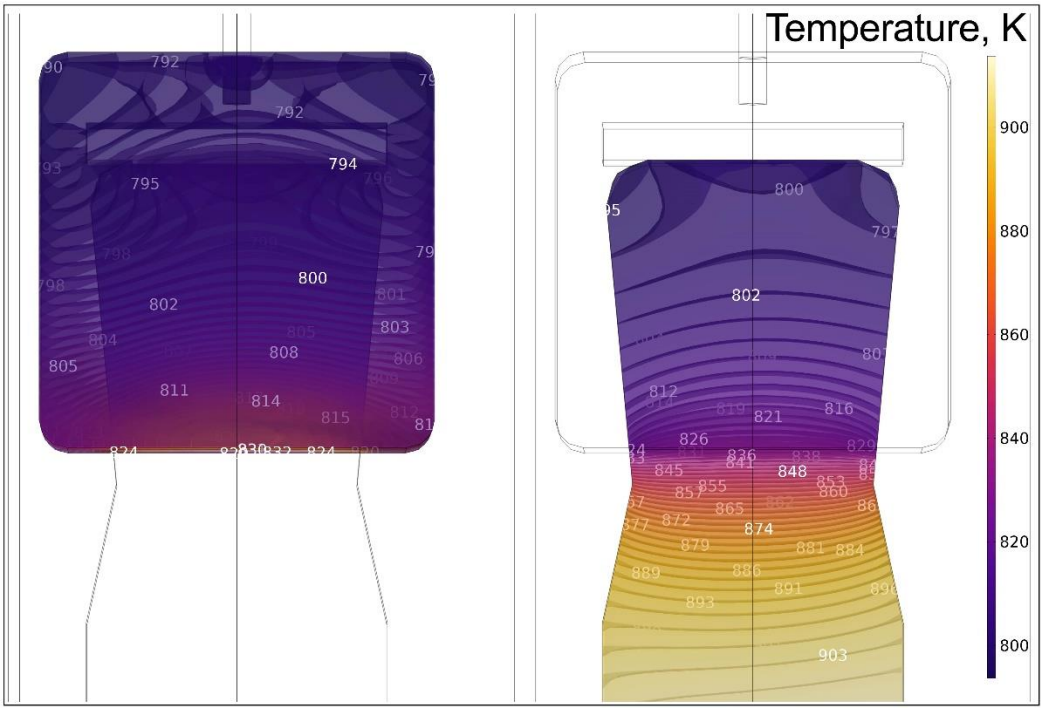


**Figure 9** Isothermal surfaces in the steady state on the anode surface and the upper current lead during the passage of a current of 50 A.

## 5. Discussion

The simulation results allowed us to identify the primary reason for the reduced lifespan of the investigated ceramic anode. This issue arises from the combination of the chosen current lead design and the differences in the electrical conductivity of the materials. The interplay of these factors promotes the development

of a temperature gradient at the three-phase boundary, consequently leading to material failure of the ceramic.

Following the analysis of the results obtained through the thermal model, a modified current lead design was proposed. The main difference of this design is that the current is supplied differently – through the upper face of the ceramic anode. In the model, the design change was reflected by introducing additional boundary conditions for the electrical problem: on the internal contact surfaces of the current lead, the electrical insulation condition was set:

$$\boldsymbol{n} \cdot \boldsymbol{j} = 0, \quad (8)$$

where $n$ is the external normal to the surface; $j$ is the electric current density. Current was supplied only through the conductive plate through the upper face of the anode.

Figure 10 shows the overall view of the fixed anode and the upper current-conducting plate on the left, while the right side depicts the internal structure of the current lead (the insulated and conductive parts are shown in gray and light purple, respectively).

The electric field distribution for the modified design of the current lead is presented in Figure 11. To assess the uniformity of current density, $j$, throughout the volume of the anode for both the old and new upper current lead designs, average values of $j$ were calculated (see Table 2) by integrating the normal current density over the volume.

Table 2 demonstrates that for the old current lead design, the average current density beneath the lead is 16 times lower than that in the free part of the anode. The implementation of the new current lead design, featuring a conductive plate adjacent to the upper face of the anode, mitigates this disparity and achieves a nearly uniform current distribution across the ceramic electrode.

Thus, the results of the simulation allow us to formulate a general principle to be followed when designing conductive structures that combine materials with significant differences in the specific electrical conductivity. According to this principle, the normal vector to the interface of materials with differing conductivity should align with the overall direction of the electric current.

An important unresolved issue remains the discrepancy between the thermal expansion coefficients of the ceramic material and the steel current lead. Due to thermal expansion during current flow, the pressure from the more ductile lead material may induce thermal stresses in the more brittle NiO-$Li_2O$ ceramic. The problems

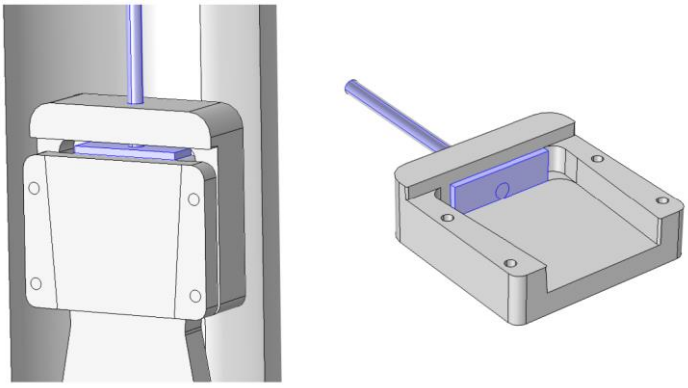

**Figure 10** Modified current lead design for the NiO-$Li_2O$ ceramic anode. The conductive part is highlighted in light purple.

**Table 2** – Current density value on the anode domain.

| Current, A | Anode average current density, A/m² | | | |
|---|---|---|---|---|
| | Old Design | | New Design | |
| | Under current lead | Free part | Under current lead | Free part |
| 10 | $7.62 \cdot 10^2$ | $1.23 \cdot 10^4$ | $1.32 \cdot 10^4$ | $1.23 \cdot 10^4$ |
| 20 | $1.52 \cdot 10^3$ | $2.46 \cdot 10^4$ | $2.64 \cdot 10^4$ | $2.46 \cdot 10^4$ |
| 30 | $2.28 \cdot 10^3$ | $3.69 \cdot 10^4$ | $3.97 \cdot 10^4$ | $3.69 \cdot 10^4$ |
| 40 | $3.05 \cdot 10^3$ | $4.93 \cdot 10^4$ | $5.29 \cdot 10^4$ | $4.93 \cdot 10^4$ |
| 50 | $3.81 \cdot 10^3$ | $6.16 \cdot 10^4$ | $6.62 \cdot 10^4$ | $6.16 \cdot 10^4$ |

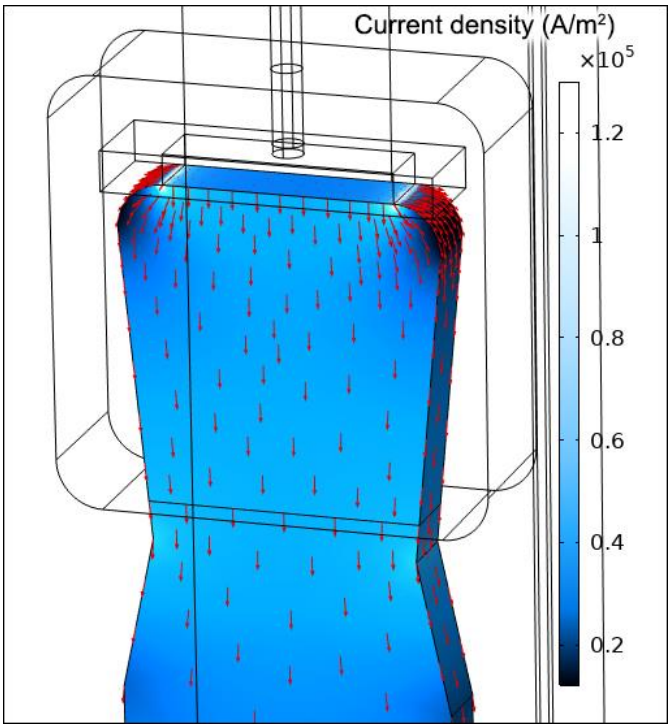


**Figure 11** Current density distribution within the anode for the modified current lead design when a current of 20 A is applied. The red arrows indicate the dispersion of current density throughout the volume of the electrode.

associated with thermal and chemical expansion of ceramics when used as electrode materials currently are of great interest [22, 23]. As noted in [22], the issue of material cracking can be partially addressed in the following ways: 1) optimizing heating parameters for the ceramic sample–heating should not be rapid; 2) controlling the isotropy of properties during the fabrication and sintering of the ceramic; 3) eliminating moisture and organic compounds from the atmosphere, which, when exposed to high temperatures, may react with the ceramic material and lead to structural changes, consequently resulting in expansion/compression effects of the original crystalline lattice. Thus, the specific challenges associated with working with ceramics necessitate the development of alternative approaches when assembling anode assemblies in electrolyzers.

Questions related to the thermal expansion of materials and their mechanical stability are subjects for further research, following which the existing model will be refined and supplemented.

## 6. Conclusions

Utilizing the tools of the COMSOL Multiphysics software package, a mathematical model has been developed to simulate the behavior of the ceramic (NiO-$Li_2O$) anode under the conditions of an experimental cell. This model allows for the calculation of thermal and electrical field distributions within the electrode while passing electric currents of various magnitudes (10–50 A). A series of thermal tests on the anode in a laboratory cell has been conducted. The developed model has been successfully validated against the experimental data, with the temperature discrepancies on the anode between the experimental and modeled results not exceeding 3 %. The calculated values of current density, as well as the temperature fields within the considered anode assembly design, may indicate that the corresponding processes contribute to the cracking at the anode/current lead/gas phase interface. Due to the differences in the specific electrical conductivity between the lead and electrode materials, the maximum temperature gradient develops precisely at this location, leading to the failure of the ceramic anode material. Analyzing the model results has allowed for the proposal of a modified current lead design. This design involves current delivery through a conductive plate adjacent to the upper face of the anode. Calculations indicate that this new design mitigates the 16-fold difference in current density values beneath the current lead and in the free part of the anode. Consequently, the improved design ensures a more uniform current density distribution within the anode and eliminates local overheating.

## Supplementary materials

This manuscript contains supplementary materials, which are available on a corresponding online page.

## Funding

This research had no external funding.

## Acknowledgments

None.

## Author contributions

Ksenia Abramova: Conceptualization; Investigation; Data curation; Methodology; Visualization; Writing – Original draft; Writing – Review & Editing.

Andrey Anisimov: Investigation; Data curation; Visualization; Writing – Review & Editing.

Oksana Rakhmanova: Data curation; Formal Analysis; Writing – Review & Editing.

Dmitry Maksimov: Conceptualization; Validation; Data curation; Formal Analysis.

Alexander Kosov: Investigation; Data curation; Writing – Original draft.

Yuri Mochalov: Methodology; Project administration.

Sergei Nikiforov: Methodology; Writing – Review & Editing.

Yuri Zaikov: Funding acquisition; Project administration; Supervision.

## Conflict of interest

The authors declare no conflict of interest.

## Additional information

Ksenia Abramova, Scopus ID: 57191836868; Orcid: 0000-0001-6521-1966;

Andrey Anisimov, Orcid: 0009-0008-9424-0326;

Oksana Rakhmanova, Scopus ID: 8619676200; Orcid: 0000-0001-6605-1626;

Dmitry Maksimov, Scopus ID: 56850160300; Orcid: 0000-0003-4448-8848;

Alexander Kosov, Scopus ID: 7004234307; Orcid: 0000-0002-7013-8991;

Yuri Mochalov, Scopus ID: 57200191291;

Yuri Zaikov, Scopus ID: 6603601069; Orcid: 0000-0001-6138-3955.

## References

1. Zhitkov A, Potapov A, Karimov K, Shishkin V, et al., Interaction between UN and $CdCl_2$ in molten LiCl-KCl eutectic.

I. Experiment at 773 K, Nucl. Eng. Technol., **52** (2020) 123e134. https://doi.org/10.1016/j.net.2019.07.006

2. Fujita R, Pyrochemical Process in Molten Salts for Spent Nuclear Fuel Reprocessing and Radioactive Waste Treatments, ECS Trans., **86** (2018) 311–320. https://doi.org/10.1149/08614.0311ecst

3. Kim S-W, Jeon MK, Kang HW, Lee S-K, et al., Carbon anode with repeatable use of LiCl molten salt for electrolytic reduction in pyroprocessing, J. Radioanal. Nucl. Chem., **310** (2016) 463e467. https://doi.org/10.1007/s10967-016-4786-5

4. Shishkin AV, Shishkin VYu, Salyulev AB, Kesikopulos VA, et al., Electrochemical reduction of uranium dioxide in LiCl–$Li_2O$ melt, Atomic Energy, **131(2)** (2021) 77–82. https://doi.org/10.1007/s10512-022-00850-y

5. Mullabaev AR, Kovrov VA, Kholkina AS, Zaikov YuP, Anode processes on Pt and ceramic anodes in chloride and oxidechloride melts, Nucl. Eng. Tech., **54** (2022) 965e974. https://doi.org/10.1016/j.net.2021.08.034

6. Yang Y-J, Yang L, Wang H-K, Zhu Sh-P, et al., Finite Element Analysis for Turbine Blades with Contact Problems, Int. J. Turbo Jet Eng., **4** (2015) 132–145. https://doi.org/10.1515/tjj-2015-0043

7. Takle ES, Russell RD, Applications of the finite element method to modeling the atmospheric boundary layer, Comp. Math. Appl., **16(1–2)** (1988) 57–68. https://doi.org/10.1016/0898-1221(88)90024-7

8. Talal MM, Sarraf ZSh, Jamil SM, Finite Element Simulation and Stress Analysis of Gas Turbine Blade Due to Centrifugal Force, Int. J. Adv. Nat. Scie. Eng. Res., **7(6)** (2023) 250–255. https://doi.org/10.59287/ijanser.1161

9. Jung H-W, Kim S-J, Kim Y-J, Kim J-Y, et al., Finite element analysis of vertical micro-probe considering Joule-heating effect, Int. J. Fat., **101(1)** (2017) 96–105. https://doi.org/10.1016/j.ijfatigue.2017.02.021

10. Liu Ch, Kelly RG, The Use of Finite Element Methods (FEM) in the Modeling of Localized Corrosion, Electrochem. Soc. Interface, **23** (2014) 47–55. https://doi.org/10.1149/2.F02144IF

11. Catalan-Martinez D, Navarrete L, Tarach M, Santos-Blasco J, et al., Thermo-fluid dynamics modelling of steam electrolysis in fully-assembled tubular high-temperature proton-conducting cells, International Journal of Hydrogen Energy, **47(65)** (2022) 27787–27799, https://doi.org/10.1016/j.ijhydene.2022.06.112

12. Necheporenko I, Arkhipov A. Modelling of the magnetic field and magnetohydrodynamic behaviour of a typical aluminium cell using COMSOL. In: Proceedings of the 2014 COMSOL Conference; 2014; p. 125.

13. Chen Yu, Yang L, Guo F, Liu D, et al., Mechanical-electrochemical modeling of silicon-graphite composite anode for lithium-ion batteries, J. Pow. Sour., **527** (2022) 231178. https://doi.org/10.1016/j.jpowsour.2022.231178

14. Mansouri A, Binali A, Khan N, Zamanzadeh M, Taheri P, Three-dimensional modeling of in-ground cathodic protection systems with deforming anodes, Sci. Rep., **11** (2021) 1894. https://doi.org/10.1038/s41598-021-81184-w

15. Chen D, Daoud H, Dörflinger T, Näser P, et al., Simulation assisted design and manufacturing of anode for the hard chrome plating of components with complex geometry, Surf. Coat. Tech., **455** (2023) 129178. https://doi.org/10.1016/j.surfcoat.2022.129178

16. Rosebrock C, Bracke S. Simulation of anode corrosion in the electrowinning process of non-ferrous metals. In: Proceedings of 2020 Annual Reliability and Maintainability Symposium (RAMS); 2020 January 27–30; Palm Springs, CA, USA. pp. 1–6. https://doi.org/10.1109/RAMS48030.2020.9153626

17. https://www.comsol.com/, COMSOL Multiphysics, v. 5.3.

18. Incropera FP, DeWitt DP, Bergman TL, Lavine AS. Fundamentals of Heat and Mass Transfer. 6th ed. New York: John Wiley & Sons; 2006. 997 p.

19. Houda S, Belarbi R, Zemmouri N, A CFD Comsol model for simulating complex urban flow, Energy Procedia, **139** (2017) 373–378. https://doi.org/10.1016/j.egypro.2017.11.224

20. Cherkasov SG, Ananyev A, Moiseeva LA, Limitations of the Boussinesq model on the example of laminary natural convection of gas between vertical isothermal walls, High Temp., **56(6)** (2018) 878. https://doi.org/10.1134/S0018151X18060081

21. Moench S, Dittrich R, Influence of Natural Convection and Volume Change on Numerical Simulation of Phase Change Materials for Latent Heat Storage, Energies, **15** (2022) 2746. https://doi.org/10.3390/en15082746

22. Loken A, Ricote S, Wachowski S, Thermal and Chemical Expansion in Proton Ceramic Electrolytes and Compatible Electrodes, Crystals, **8(9)** (2018) 365. https://doi.org/10.3390/cryst8090365

23. Sofie SW, Taylor DR. Controlled Thermal Expansion Anode Compositions with Improved Strength for Use in Anode Supported SOFCs. New York: John Wiley & Sons, Inc.; 2009. pp. 215–223. https://doi.org/10.1002/9780470339534.ch21